

# Relativistic calculations of angular dependent photoemission time delay

Anatoli Kheifets\*

Research School of Physics and Engineering, The Australian National University, Canberra ACT 0200, Australia

Ankur Mandal† and Pranawa C. Deshmukh‡

Department of Physics, Indian Institute of Technology Madras, Chennai, Tamil Nadu 600036, India

Valeriy K. Dolmatov§

Department of Physics and Earth Science, University of North Alabama, Florence, AL 35632, USA

David A. Keating¶ and Steven T. Manson\*\*

Department of Physics and Astronomy, Georgia State University, Atlanta, GA 30303, USA

(Dated: July 2, 2021)

Angular dependence of photoemission time delay for the valence  $np_{3/2}$  and  $np_{1/2}$  subshells of Ar, Kr and Xe is studied in the dipole relativistic random phase approximation. Strong angular anisotropy of the time delay is reproduced near respective Cooper minima while the spin-orbit splitting affects the time delay near threshold.

PACS numbers: 32.80.Rm, 32.80.Fb, 42.50.Hz

## I. INTRODUCTION

A measurable time delay in laser driven atomic ionization has been discovered recently [1, 2]. Since the first pioneering experiments, the time-delay spectroscopy of laser-induced atomic ionization (attosecond chronoscopy) has become a rapidly developing field [3]. Among other characteristic features, an angular anisotropy of attosecond time delay relative to polarization of laser light has been predicted theoretically [4, 5] and measured experimentally [6]. In one-photon photoionization of atomic  $np$  subshells, the time delay can show some angular anisotropy due to the interplay of the  $\epsilon s$  and  $\epsilon d$  photoelectron continua [4, 5]. This anisotropy becomes particularly strong near a Cooper minimum in the dominant  $np \rightarrow \epsilon d$  channel, making the nominally weak  $np \rightarrow \epsilon s$  channel competitive. In two-color (two-photon) XUV/IR experiments, the interference of these photoemission channels can manifest itself even in a spherically symmetric  $ns$  atomic subshell. This leads to a strong angular anisotropy of the measured time delay when the  $\epsilon d$  continuum has a kinematic node near the magic angle of  $54.7^\circ$ . Such a strong anisotropy has indeed been measured in He in a recent RABBITT (Reconstruction of Attosecond Beating By Interference of Two-photon Transitions) experiment [6]. Another interesting aspect of photoemission time delay is its sensitivity to the fine structure of the ionized target. Recent experiments have detected such a sensitivity in the valence shell photoionization of the Kr and Xe atoms [7].

In this paper, we investigate both the angular and spin dependence of the time delay using the dipole relativistic random phase approximation (RRPA). We expand our previous relativistic studies of the time delay [8, 9]

and include the full interference of all the spin-orbit coupled photoionization channels. In the previous studies, only the time delay in the dominant channel was evaluated. We validate our theoretical model using the angular dependent time delay near the Cooper minimum of the  $3p$  subshell of Ar. For the relatively light Ar atom, our RRPA results agree very well with non-relativistic random-phase approximation with exchange (RPAE) <sup>1</sup> calculations [4]. For heavier Kr and Xe atoms, we clearly observe the manifestation of relativistic effects. One such effect is a spin-orbit splitting of the time delay near threshold.

The paper is organized as follows. In Sec. II a brief theoretical formulation is given. In section III the results for the angle and energy dependence of Wigner time delay for photoemission from outer  $np_{1/2}$  and  $np_{3/2}$  subshells of atomic Ar, Kr and Xe are presented and discussed; Ne is omitted because there is no Cooper minimum in its photoionization cross section. Conclusions are drawn in section IV.

## II. THEORETICAL METHOD

### A. Photoionization amplitude

We adopt the multichannel RRPA formalism of Johnson and Lin [11]. In this formalism, the amplitude for a transition from the ground state ( $u_i$ ) to an excited state ( $\omega_{i\pm}$ ), induced by a time varying external field  $v_+ e^{-i\omega t} + v_- e^{i\omega t}$  is given by

$$T = \sum_{i=1}^N \int d^3r (\omega_{i+}^\dagger \vec{\alpha} \cdot \vec{A} u_i + u_i^\dagger \vec{\alpha} \cdot \vec{A} \omega_{i-}) . \quad (1)$$

Here the electromagnetic interaction is written in Coulomb gauge and expressed in terms of the Pauli spin

\*Electronic address: a.kheifets@anu.edu.au

†Electronic address: amankur@physics.iitm.ac.in

‡Electronic address: pcd@physics.iitm.ac.in

§Electronic address: vkdolmatov@una.edu

¶Electronic address: dkeating2@student.gsu.edu

\*\*Electronic address: smanson@gsu.edu

<sup>1</sup> The same exchange interaction is accounted for both in the RPAE and RRPA but E is dropped from the latter acronym for brevity.

matrices  $\vec{\alpha} = \begin{pmatrix} 0 & \vec{\sigma} \\ \vec{\sigma} & 0 \end{pmatrix}$  and the vector potential  $\vec{A}$ .

In a single active electron approximation, the multipole transition amplitude is reduced to

$$T_{JM}^{(\lambda)} = \int d^3r \omega_{i+}^\dagger \vec{\alpha} \cdot \vec{a}_{JM}^\lambda u_i, \quad (2)$$

where the indices  $J$  and  $M$  are the photon angular momentum and its projection and  $\lambda = 1$  or  $0$  for electric or magnetic multipoles, respectively. Specifically, for a one-electron transition from an initial state characterized by the quantum numbers  $ljm$  to a final continuum state  $\bar{l}\bar{j}\bar{m}$  with the spin described by a two-component spinor  $\chi_\nu$ , this equation becomes

$$T_{JM}^{(\lambda)} = i \sqrt{\frac{2\pi^2}{Ep}} \sqrt{\frac{(2J+1)(J+1)}{J}} \frac{\omega^J}{(2J+1)!!} \\ \times \sum_{\bar{\kappa}\bar{m}} (\chi_\nu^\dagger \Omega_{\bar{\kappa}\bar{m}}(\hat{p})) (-1)^{\bar{j}-\bar{m}} \begin{pmatrix} \bar{j} & J & j \\ -\bar{m} & M & m \end{pmatrix} \\ \times i^{1-\bar{l}} e^{i\delta_{\bar{\kappa}}} \langle \bar{a} \| Q_J^{(\lambda)} \| a \rangle (-1)^{\bar{j}+j+J}. \quad (3)$$

Here  $E$  and  $\hat{p}$  are the photoelectron energy and momentum direction, respectively,  $\omega$  is the photon frequency,  $\delta_{\bar{\kappa}}$  is the phase of the continuum wave with  $\bar{\kappa} = \mp(\bar{j} + \frac{1}{2})$  for  $\bar{j} = (\bar{l} \pm \frac{1}{2})$ . The spherical spinor is defined as

$$\Omega_{\kappa m}(\hat{n}) = \sum_{\nu=\pm 1/2} C_{l,M-\nu,1/2\nu}^{jM} Y_{lm-\nu}(\hat{n}) \chi_\nu \quad (4)$$

The corresponding Clebsch-Gordan coefficients are tabulated in [12]. The reduced matrix element of the spherical tensor between the initial state  $a = (n\kappa)$  and a final energy scale normalized state  $a = (E, \bar{\kappa})$  is written as

$$\langle \bar{a} \| Q_J^{(\lambda)} \| a \rangle = (-1)^{j+1/2} [\bar{j}] [j] \begin{pmatrix} j & \bar{j} & J \\ -1/2 & 1/2 & 0 \end{pmatrix} \\ \times \pi(\bar{l}, l, J-l+1) R_J^{(l)}(\bar{a}, a) \quad (5)$$

Here  $\pi(\bar{l}, l, J-l+1) = 1$  or  $0$  for  $\bar{l}+l+J-l+1$  even or odd, respectively, and  $R_J^{(l)}(\bar{a}, a)$  is the radial integral. While Eq. (5) is derived for a single-electron transition, it also applies to closed-shell atomic systems. In order to include the RRPA correlations, the only change in Eq. (3) is to replace  $\langle \bar{a} \| Q_J^{(\lambda)} \| a \rangle$  with  $\langle \bar{a} \| Q_J^{(\lambda)} \| a \rangle_{\text{RRPA}}$ . Finally, as we will be dealing with electric dipole photoionizing transitions, we set  $l = 1$ ,  $J = 1$  and choose  $M = 0$  which corresponds to linear polarization in the  $z$ -direction. In this case, Eq. (3) is reduced to

$$T_{10}^{1\pm} \equiv [T_{10}^{(1)}]_{\nu=\pm 1/2} = \sum_{\bar{\kappa}\bar{m}} C_{l,M-\nu,1/2\nu}^{jM} Y_{lm-\nu}(\hat{p}) \chi_\nu \\ \times (-1)^{\bar{j}+j+1+\bar{j}-\bar{m}} \begin{pmatrix} \bar{j} & 1 & j \\ -\bar{m} & 0 & m \end{pmatrix} i^{1-\bar{l}} e^{i\delta_{\bar{\kappa}}} \langle \bar{a} \| Q_1^{(1)} \| a \rangle \quad (6)$$

Here we dropped the common scaling factor for brevity of notation. We will also be using a shorthand for a reduced matrix element modified by the phase factors:

$$D_{l_j \rightarrow \bar{l}\bar{j}} = i^{1-\bar{l}} e^{i\delta_{\bar{\kappa}}} \langle \bar{a} \| Q_J^{(\lambda)} \| a \rangle \quad (7)$$

We note that Eq. (3) differs by the extra parity factor  $(-1)^{\bar{j}+j+J}$  from the original equation (43) of Johnson and Lin [11]. We added this factor to make it comply with the Wigner-Eckart theorem (Eq. 107-6 of Landau and Lifshitz [13]).

## B. Formulation of angular dependent time delay

An electric dipole transition from a  $np$  initial state leads to the following five ionization channels:

$$np_{1/2} \rightarrow \epsilon s_{1/2}, \epsilon d_{3/2} \\ np_{3/2} \rightarrow \epsilon s_{1/2}, \epsilon d_{3/2}, \epsilon d_{5/2}$$

Using Eq. (6), we derive the following expressions for the  $np_{1/2}$  ionization amplitude:

$$[T_{10}^{1+}]_{np_{1/2}}^{m=\frac{1}{2}} = + \frac{1}{\sqrt{15}} Y_{20} D_{np_{1/2} \rightarrow \epsilon d_{3/2}} + \frac{1}{\sqrt{6}} Y_{00} D_{np_{1/2} \rightarrow \epsilon s_{1/2}} \\ [T_{10}^{1-}]_{np_{1/2}}^{m=\frac{1}{2}} = - \frac{1}{\sqrt{10}} Y_{21} D_{np_{1/2} \rightarrow \epsilon d_{3/2}}$$

Here and throughout the text,  $Y_{l,m} \equiv Y_{lm}(\hat{p})$ . The corresponding amplitudes with the  $m = -1/2$  projection will have a similar structure with the simultaneous inversion of the spin projection  $T^+ \leftrightarrow T^-$  and the second index of the spherical harmonic  $Y_{21} \rightarrow Y_{2-1}$ . Each amplitude has its own associated photoelectron group delay (the Wigner time delay [14]) defined as

$$\tau = \frac{d\eta}{dE}, \quad \eta = \tan^{-1} \left[ \frac{\text{Im} T_{10}^{1\pm}}{\text{Re} T_{10}^{1\pm}} \right]. \quad (8)$$

The spin averaged time delay can be expressed as a weighted sum

$$\bar{\tau}_{np_{1/2}} = \frac{\tau_{np_{1/2}}^{m=\frac{1}{2},+} \left| [T_{10}^{1+}]_{np_{1/2}}^{m=\frac{1}{2}} \right|^2 + \left| [T_{10}^{1-}]_{np_{1/2}}^{m=\frac{1}{2}} \right|^2 \tau_{np_{1/2}}^{m=\frac{1}{2},-}}{\left| [T_{10}^{1+}]_{np_{1/2}}^{m=\frac{1}{2}} \right|^2 + \left| [T_{10}^{1-}]_{np_{1/2}}^{m=\frac{1}{2}} \right|^2} \quad (9)$$

The angular resolved amplitudes for the  $np_{3/2}$  initial state take the following form:

$$[T_{10}^{1+}]_{np_{3/2}}^{m=1/2} = \frac{1}{\sqrt{6}} Y_{00} D_{np_{3/2} \rightarrow \epsilon s_{1/2}} - \frac{1}{5\sqrt{6}} Y_{20} D_{np_{3/2} \rightarrow \epsilon d_{3/2}} \\ - \frac{1}{5} \sqrt{\frac{3}{2}} Y_{20} D_{np_{3/2} \rightarrow \epsilon d_{5/2}} \\ [T_{10}^{1-}]_{np_{3/2}}^{m=1/2} = \frac{1}{10} Y_{21} D_{np_{3/2} \rightarrow \epsilon d_{3/2}} - \frac{1}{5} Y_{21} D_{np_{3/2} \rightarrow \epsilon d_{5/2}} \\ [T_{10}^{1+}]_{np_{3/2}}^{m=3/2} = - \frac{\sqrt{3}}{10} Y_{21} D_{np_{3/2} \rightarrow \epsilon d_{3/2}} - \frac{2\sqrt{3}}{15} Y_{21} D_{np_{3/2} \rightarrow \epsilon d_{5/2}} \\ [T_{10}^{1-}]_{np_{3/2}}^{m=3/2} = \frac{\sqrt{3}}{5} Y_{22} D_{np_{3/2} \rightarrow \epsilon d_{3/2}} - \frac{\sqrt{3}}{15} Y_{22} D_{np_{3/2} \rightarrow \epsilon d_{5/2}}$$

The corresponding spin averaged time delay becomes

$$\mathcal{S} \times \bar{\tau}_{np_{3/2}} = \tau_{np_{3/2}}^{m=\frac{1}{2},+} \left| [T_{10}^{1+}]_{np_{3/2}}^{m=\frac{1}{2}} \right|^2 + \tau_{np_{3/2}}^{m=\frac{1}{2},-} \left| [T_{10}^{1-}]_{np_{3/2}}^{m=\frac{1}{2}} \right|^2 \\ + \tau_{np_{3/2}}^{m=\frac{3}{2},+} \left| [T_{10}^{1+}]_{np_{3/2}}^{m=\frac{3}{2}} \right|^2 + \tau_{np_{3/2}}^{m=\frac{3}{2},-} \left| [T_{10}^{1-}]_{np_{3/2}}^{m=\frac{3}{2}} \right|^2 \\ \text{with } \mathcal{S} = \left| [T_{10}^{1+}]_{np_{3/2}}^{m=\frac{1}{2}} \right|^2 + \left| [T_{10}^{1-}]_{np_{3/2}}^{m=\frac{1}{2}} \right|^2 \\ + \left| [T_{10}^{1+}]_{np_{3/2}}^{m=\frac{3}{2}} \right|^2 + \left| [T_{10}^{1-}]_{np_{3/2}}^{m=\frac{3}{2}} \right|^2$$

Here we restricted ourselves to positive  $m = 1/2, 3/2$ . The corresponding time delay with negative  $m$  will be identical.

### C. Non-relativistic limit

Using Eqs. (5) and (7), we can express the amplitudes via the corresponding radial integrals modified by the phase factors. For a mildly relativistic atom, the radial integrals with  $\bar{j} = \bar{l} \pm 1/2$  orbitals will be very similar. Hence we can neglect this difference and reduce the amplitudes to the following expressions:

$$T_{10}^{1+}(np_{1/2}) = -\frac{1}{3}Y_{00}R_{np \rightarrow \epsilon s} - \frac{2}{3}\frac{1}{\sqrt{5}}Y_{20}R_{np \rightarrow \epsilon d}$$

$$T_{10}^{1+}(np_{3/2}) = \frac{\sqrt{2}}{3}Y_{00}R_{np \rightarrow \epsilon s} + \frac{2}{3}\sqrt{\frac{2}{5}}Y_{20}R_{\epsilon d}$$

$$T_{10}^{1-}(np_{1/2}) = \sqrt{\frac{2}{15}}Y_{21}R_{np \rightarrow \epsilon d}$$

$$T_{10}^{1-}(np_{3/2}) = \sqrt{\frac{1}{15}}Y_{21}R_{np \rightarrow \epsilon d}$$

This is to be compared with the corresponding non-relativistic amplitudes [15]

$$T_{npm=0 \rightarrow \epsilon s} = \frac{1}{\sqrt{3}}Y_{00}(\hat{n})R_{np \rightarrow \epsilon s}$$

$$T_{npm=0 \rightarrow \epsilon d} = 2\sqrt{\frac{1}{15}}Y_{20}(\hat{n})R_{np \rightarrow \epsilon d}$$

$$T_{npm=1 \rightarrow Ed} = -\sqrt{\frac{1}{5}}Y_{21}(\hat{n})R_{np \rightarrow Ed}$$

By comparing the weakly relativistic and strictly non-relativistic amplitudes, we can observe the following scaling properties:

$$\begin{aligned} [T^+]_{np_{1/2}}^{m=1/2} &\simeq \frac{1}{\sqrt{3}}T_{npm=0} & [T^-]_{np_{1/2}}^{m=1/2} &\simeq -\sqrt{\frac{2}{3}}T_{npm=1} \\ [T^+]_{np_{3/2}}^{m=1/2} &\simeq \sqrt{\frac{2}{3}}T_{npm=0} & [T^-]_{np_{3/2}}^{m=1/2} &\simeq -\frac{1}{\sqrt{3}}T_{npm=1} \\ [T^+]_{np_{3/2}}^{m=3/2} &\simeq T_{npm=1} & [T^-]_{np_{3/2}}^{m=3/2} &\simeq 0 \end{aligned} \quad (10)$$

By feeding this scaling into the spin-averaged time delay expressions, we get

$$\bar{\tau}_{np_{1/2}} = \frac{\tau_{npm=0}|T_{npm=0}|^2 + 2\tau_{npm=1}|T_{npm=1}|^2}{|T_{npm=0}|^2 + 2|T_{npm=1}|^2} \simeq \bar{\tau}_{np},$$

which represents the magnetic projection average non-relativistic time delay as is used in [4]. By the same token,

$$\bar{\tau}_{np_{3/2}} = \frac{2\tau_{npm=0}|T_{npm=0}|^2 + 4\tau_{npm=1}|T_{npm=1}|^2}{2|T_{npm=0}|^2 + 4|T_{npm=1}|^2} \simeq \bar{\tau}_{np}$$

### III. RESULTS AND DISCUSSION

The RRPA calculations have been performed with the following channels coupled: 14 channels for Ar (all dipole excitations from the  $3p$ ,  $3s$  and  $2p$  subshells), 18 channels for Kr (excitations from the  $4p$ ,  $4s$ ,  $3d$  and  $3p$  subshells) and 18 channels for Xe (the  $5p$ ,  $5s$ ,  $4d$  and  $4p$  subshells). In addition, where available, experimental threshold energies from [16] were used to facilitate better comparison with experiment. These energies are identical to those displayed in Table 1 of [8].

### A. Argon

Argon is hardly a relativistic target and only chosen here for validation and calibration of our theoretical model against the previous calculations [4, 5] and experiment [17]. The time delay of Ar  $3p_{1/2}$  and  $3p_{3/2}$  subshells in the energy range encompassing the Cooper minimum is shown in Fig. 1 for the fixed emission angles  $\theta = 0^\circ$  (top panel) and  $\theta = 45^\circ$  (middle panel). Comparison is made with the non-relativistic RPAE calculations [4, 15] and the exterior complex scaling (ECS) calculation [5]. The bottom panel displays the angular averaged result where a comparison is also shown with a RABBITT experiment [17] in which no discrimination with the photoelectron direction was made.

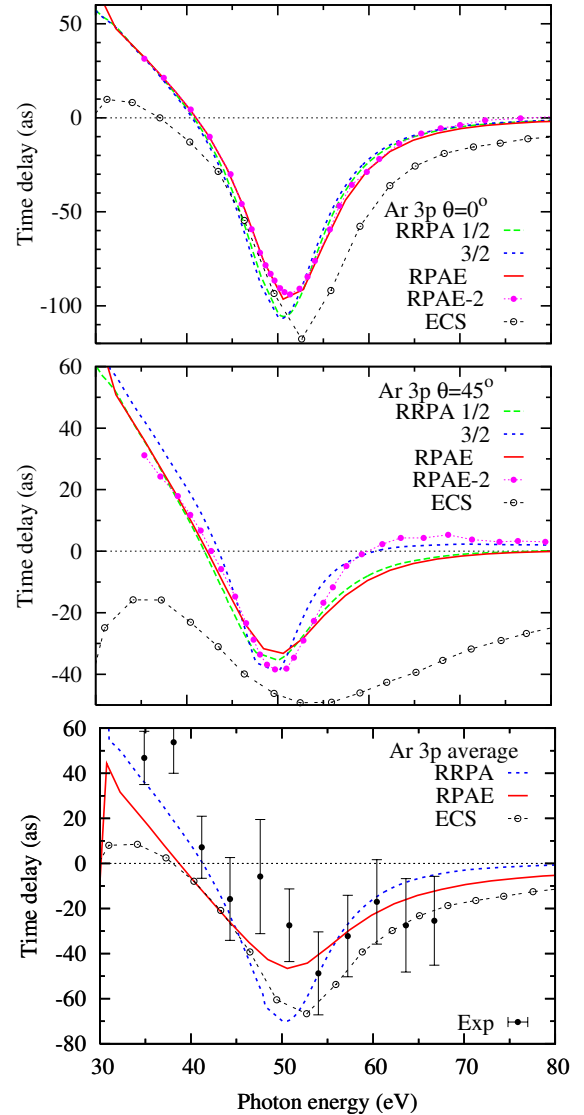


FIG. 1: (Color online) The time delay of Ar  $3p_{1/2}$  (green dashed line) and  $3p_{3/2}$  (blue dotted line) is plotted versus the photon energy. The nonrelativistic RPAE results from Ref. [15] and RPAE-2 from [4] are shown by the red solid line and filled circles, respectively. The top panel:  $\theta = 0^\circ$ , middle panel:  $\theta = 45^\circ$ , bottom panel: angular average. The experimental data from [17] are shown on the bottom panel with error bars.

In the polarization direction at  $\theta = 0^\circ$ , the present

RRPA results and non-relativistic RPAE [4, 15] results agree very well. Not surprisingly, there is very little difference in the time delay between the  $3p_{1/2}$  and  $3p_{3/2}$  subshells in Ar, indicating that the spin-orbit interaction is unimportant here. The ECS calculation [5] differs noticeably. This may be attributed to a different methodology of the time delay determination in this work. Indeed, all the RRPA and RPAE calculations were performed for single-photon XUV photoionization. Hence it is the Wigner time delay that was evaluated in the present work. In the ECS calculation [5], the time delay was computed using correlated two-photon (XUV+IR) above threshold matrix elements [18]. In such a definition, the atomic time delay contains the so-called Coulomb-laser coupling (CLC) correction.

$$\tau_a = \tau_W + \tau_{CLC}, \quad (11)$$

This correction is known to decrease rapidly with a growing photoelectron energy and is relatively small near the Cooper minimum. However, it is large near threshold and will be accounted for in our calculations presented in the next section. At the fixed photoelectron emission angle  $\theta = 45^\circ$  (middle panel), the RPAE results [4, 15] and the present RRPA calculation are still rather close. However, the ECS calculation is considerably further away than in the case of  $\theta = 0^\circ$ . This deviation can be possibly attributed to further suppression of the  $\epsilon d$  continuum because of the kinematic node of the  $f$ -wave close to  $45^\circ$ . We note that the  $\epsilon d$  continuum is converted to the  $p$ - and  $f$ -waves by the IR photon absorption in two-color photoionization experiments. When the angular average is taken (bottom panel), the difference between all the calculations is not so pronounced and they compare reasonably well with the experiment [17]. A more accurate angular resolved measurement is needed to validate various theoretical predictions in the directions away from the polarization axis.

## B. Krypton and xenon

The time delay of Kr  $4p_{1/2}$  and  $4p_{3/2}$  subshells in the energy range encompassing the Cooper minimum is shown in Fig. 2 in the two fixed directions  $\theta = 0^\circ$  and  $\theta = 45^\circ$ . The time delay displays the characteristic dip near the Cooper minimum but not as deep as in the case of argon. The depth of the minimum indicates the relative strength of the nominally weaker channel near the Cooper minimum of the normally stronger channel. In the non-relativistic RPAE model, this stronger channel can be identified with the  $4p_{m=0} \rightarrow \epsilon d$  transition. Other angular momentum projections  $m = \pm 1$  in this channel are excluded in the  $\theta = 0^\circ$  polarization direction. Away from this direction, weaker channels  $4p_{m=\pm 1} \rightarrow \epsilon d$ , along with the  $4p_{m=0} \rightarrow \epsilon s$  channel, also make their contribution to the photoionization amplitude and the time delay. Hence the Cooper minimum in the time delay is getting shallower. Overall the angular dependence is much weaker in Kr than in the case of Ar. Nevertheless, the RRPA calculations show a noticeable deviation from the RPAE and the spin-orbit splitting of the time delay becomes visible.

The analogous set of data for the Xe  $5p_{1/2}$  and  $5p_{3/2}$  subshells is shown in Fig. 3. The photon energy range

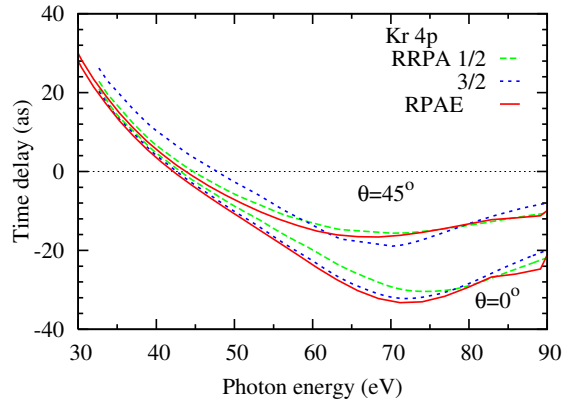


FIG. 2: The time delay of Kr  $4p_{1/2}$  (green dashed line) and  $4p_{3/2}$  (blue dotted line) is plotted versus the photon energy in the fixed emission directions  $\theta = 0^\circ$  and  $\theta = 45^\circ$ . The nonrelativistic RPAE result from Ref. [15] is shown by the red solid line. The angular averaged experimental data from [17] are shown with error bars.

near the Cooper minimum encompasses two series of autoionization resonances  $5s^1 np$  [19] and  $4d^9 np$  [20]. These resonances cause rapid oscillations of the time delay which are well resolved in the present RRPA calculation but not so well in the RPAE [15]. As in the case of Kr, the relativistic effects are noticeable in Xe. Similar to other atoms, the Cooper minimum of the time delay is flattening away from the polarization direction.

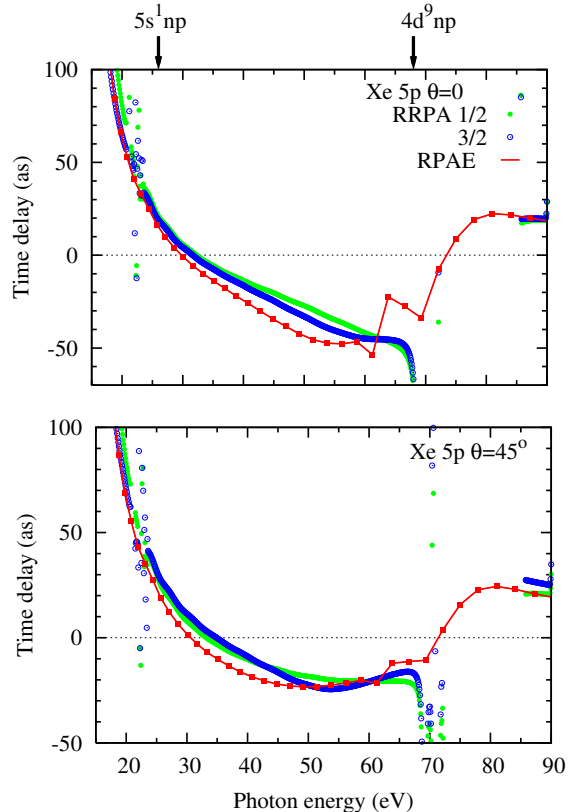


FIG. 3: The time delay of Xe  $5p_{1/2}$  (green filled circles) and  $5p_{3/2}$  (blue open circles) is plotted versus the photon energy. The nonrelativistic RPAE result from Ref. [15] is shown by the red solid line. Regions of the autoionization series  $5s^1 np$  [19] and  $4d^9 np$  [20] are marked by vertical arrows.

### C. Near threshold region

The time delay near the threshold is dominated strongly by the Coulomb singularity. The scattering phase of the photoelectron propagating in the field of the singly charged parent ion diverges to negative infinity as the photoelectron energy goes to zero [21]. Correspondingly, the photoelectron group delay (the Wigner time delay) tends to positive infinity near threshold. The CLC correction has a similar logarithmic singularity [22] but it is negative. So the total atomic time delay (11) is the sum of the two divergent terms of the opposite signs.

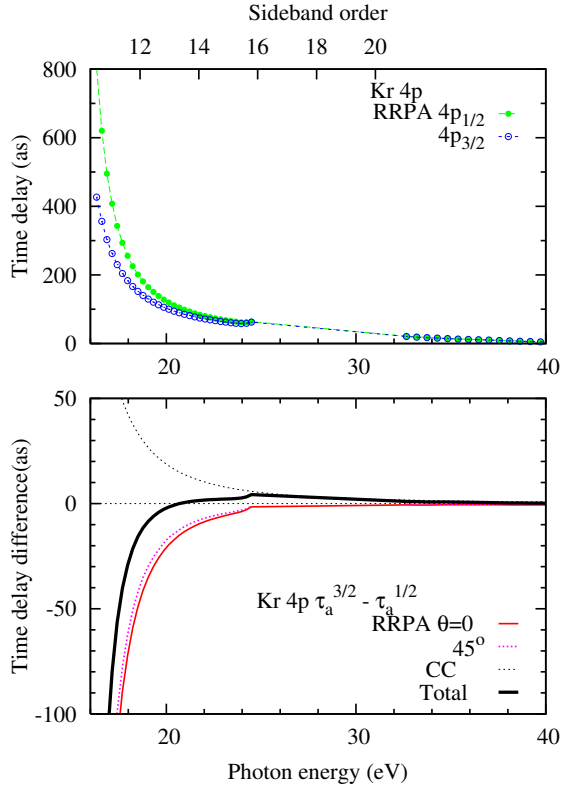


FIG. 4: The atomic time delay in the Kr 4p subshell. Top: the Wigner time delay from the  $4p_{1/2}$  and  $4p_{3/2}$  subshells is shown with filled green circles and open blue circles, respectively. Bottom: the time delay difference  $\tau_a^{3/2} - \tau_a^{1/2}$ . The raw RRPA calculations at  $\theta = 0^\circ$  and  $45^\circ$  are shown with the red solid and purple dashed lines, respectively. The CLC correction from [22] is visualized with a thin dotted line. The RRPA result corrected by the CLC is shown with a thick solid line.

In the near threshold experiment [7], it is the difference of the atomic time delays in the  $np_{1/2}$  and  $np_{3/2}$  subshells that is measured. Because of the different ionization potentials, the photoelectron ejected from the deeper  $np_{1/2}$  subshell has a smaller kinetic energy than the one ionized from the  $np_{3/2}$  subshell. Hence the Wigner time delay in the  $np_{1/2}$  subshell is larger than the  $np_{3/2}$  subshell at the same photon energy. This characteristic behavior is seen on the top panels of Fig. 4 for Kr and Fig. 5 for Xe. The same difference in the photoelectron kinetic energies will affect the respective CLC corrections to the time delay in the  $np_{1/2}$  and  $np_{3/2}$  subshells. To account for this effect, we used the values of  $\tau_{\text{CLC}}$  plotted in Fig. 5 of [22] as a function of the photoelectron energy. We fitted it with an analytical formula and calculated the difference

$\tau_{\text{CLC}}^{3/2} - \tau_{\text{CLC}}^{1/2}$  due to the difference in respective ionization potentials. The corresponding difference for the Wigner time delay  $\tau_{\text{W}}^{3/2} - \tau_{\text{W}}^{1/2}$  was extracted from the RRPA calculations. The area of the autoionization resonances was excluded from this procedure because of the rapid variation of the Wigner time delay in this region.

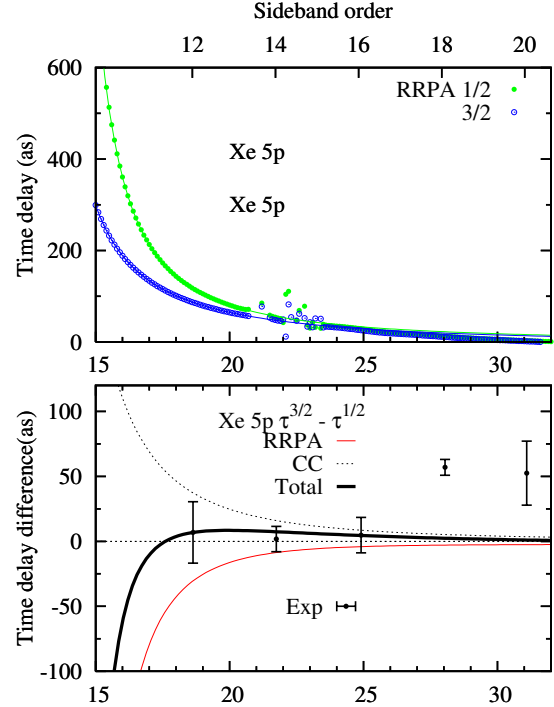


FIG. 5: Same as Fig. 4 for Xe 5p subshell. The experimental data from [7] are plotted with error bars.

The resulting values of the time delay difference are shown in the bottom panels of Fig. 4 and Fig. 5 for Kr and Xe, respectively. In the case of Kr, the angular dependence of the time delay difference  $\tau_{\text{W}}^{3/2} - \tau_{\text{W}}^{1/2}$  is small as can be seen in comparison of the values obtained for the two fixed scattering angles  $\theta = 0^\circ$  and  $\theta = 45^\circ$ . Hence the values of the atomic time delay difference  $\tau_a^{3/2} - \tau_a^{1/2}$  evaluated in the direction of the polarization axis can be compared with the angular averaged experiment [7]. In the case of Xe, this difference is even smaller and not noticeable in the scale of the bottom panel of Fig. 5.

In comparison to Kr, Xe has smaller ionization thresholds. Hence, at the same photon energy, the photoelectrons have larger kinetic energy which take them further away from the threshold. Therefore, the effect of the Coulomb singularity on the Wigner time delay and the CLC correction is weaker. The net atomic time delay difference in Xe becomes positive near threshold whereas it is negative or close to zero in the case of Kr. These findings are in line with the experiment [7].

## IV. CONCLUSIONS

We applied the relativistic formalism and RRPA computational scheme to evaluate the time delay in the valence shell of noble gas atoms, Ar, Kr and Xe. The two characteristic features of the time delay are analyzed: the angular dependence near the Cooper minimum and the

effect of the spin-orbit splitting near the threshold. Comparison with nonrelativistic calculations serves as a convenient test and a calibration tool. The effect of the spin-orbit splitting is not strong near the Cooper minimum which is relatively far away from the ionization threshold. However, the angular dependence is significant in this photon energy range due to efficient competition of the nominally weak and strong photoionization channels. This dependence is most pronounced in Ar. Indirectly, this angular dependence is confirmed by the angular integrated experiment [17] which agrees much better with angular averaged calculations rather than angular specific data. In heavier noble gases, Kr and Xe, the angular dependence also noticeable but not as pronounced as in Ar.

The time delay in the near-threshold region shows little or no angular dependence while the spin-orbit splitting effect is large. At the same photon energy, the photoelectron ejected from a deeper  $np_{1/2}$  subshell has smaller kinetic energy and less affected by the Coulomb singularity as its counterpart ejected from the shallower  $np_{3/2}$  subshell. The corresponding difference in the Wigner

time delays is offset by the difference in the correction due to the Coulomb-laser coupling. As a result, the net atomic delay difference becomes positive in Xe and remains negative in Kr. These findings are in line with recent experimental observations [7].

### Acknowledgments

The authors wish to thank Hans Jakob Wörner for many stimulating discussions and Marcus Dahlström for useful comments. ASK acknowledges support of the ARC Discovery grant DP120101805. AM wants to thank Dr. G. Aravind, Department of Physics, IIT Madras, India, for very fruitful discussion. VKD acknowledges the support of NSF under grant No. PHY-1305085. PCD acknowledges the support of a grant from the Department of Science and Technology, Government of India. STM was supported by Division of Chemical Sciences, Basic Energy Science, Office of Science US Department of Energy.

- 
- [1] M. Schultze *et al.*, *Delay in Photoemission*, *Science* **328**(5986), 1658 (2010).
- [2] K. Klünder, J. M. Dahlström, M. Gisselbrecht, T. Fordell, M. Swoboda, D. Guénot, P. Johnsson, J. Caillat, J. Mauritsson, A. Maquet, et al., *Probing single-photon ionization on the attosecond time scale*, *Phys. Rev. Lett.* **106**(14), 143002 (2011).
- [3] R. Pazourek, S. Nagele, and J. Burgdörfer, *Attosecond chronoscopy of photoemission*, *Rev. Mod. Phys.* **87**, 765 (2015).
- [4] J. Wätzel, A. S. Moskalenko, Y. Pavlyukh, and J. Berakdar, *Angular resolved time delay in photoemission*, *J. Phys. B* **48**(2), 025602 (2015).
- [5] J. M. Dahlström and E. Lindroth, *Study of attosecond delays using perturbation diagrams and exterior complex scaling*, *J. Phys. B* **47**(12), 124012 (2014).
- [6] S. Heuser, Á. Jiménez Galán, C. Cirelli, M. Sabbar, R. Boge, M. Lucchini, L. Gallmann, I. Ivanov, A. S. Kheifets, J. M. Dahlström, et al., *Time delay anisotropy in photoelectron emission from the isotropic ground state of helium*, ArXiv e-prints 1503.08966, Nat. Phys. submitted (2015), 1503.08966.
- [7] M. Huppert, I. Jordan, S. Pabst, and H. J. Wörner, *Relativistic photoionization delays and the role of auto-ionizing resonances*, *Journal of Physics: Conference Series* **635**(9), 092135 (2015).
- [8] S. Saha, A. Mandal, J. Jose, H. R. Varma, P. C. Deshmukh, A. S. Kheifets, V. K. Dolmatov, and S. T. Manson, *Relativistic effects in photoionization time delay near the Cooper minimum of noble-gas atoms*, *Phys. Rev. A* **90**, 053406 (2014).
- [9] A. S. Kheifets, S. Saha, P. C. Deshmukh, D. A. Keating, and S. T. Manson, *Dipole phase and photoelectron group delay in inner-shell photoionization*, *Phys. Rev. A* **92**, 063422 (2015).
- [10] M. Y. Amusia, *Atomic photoeffect* (Plenum Press, New York, 1990).
- [11] W. R. Johnson and C. D. Lin, *Multichannel relativistic random-phase approximation for the photoionization of atoms*, *Phys. Rev. A* **20**, 964 (1979).
- [12] D. A. Varshalovich, A. N. Moskalev, and V. K. Khersonskii, *Quantum theory of angular momentum* (World Scientific, Philadelphia, 1988), 1st ed.
- [13] L. D. Landau and E. M. Lifshitz, *Quantum Mechanics (Non-relativistic theory)*, vol. 3 of *Course of theoretical physics* (Pergamon press, Oxford, 1985), 3rd ed.
- [14] E. P. Wigner, *Lower limit for the energy derivative of the scattering phase shift*, *Phys. Rev.* **98**(1), 145 (1955).
- [15] A. S. Kheifets, *Time delay in valence-shell photoionization of noble-gas atoms*, *Phys. Rev. A* **87**, 063404 (2013).
- [16] Y. Ralchenko, A. E. Kramida, J. Reader, and NIST ASD Team, *NIST Atomic Spectra Database (version 3.1.5)*, Tech. Rep., National Institute of Standards and Technology, Gaithersburg, MD. (2011), URL <http://physics.nist.gov/asd>.
- [17] C. Palatchi, J. M. Dahlström, A. S. Kheifets, I. A. Ivanov, D. M. Canaday, P. Agostini, and L. F. DiMauro, *Atomic delay in helium, neon, argon and krypton*, *J. Phys. B* **47**(24), 245003 (2014).
- [18] J. M. Dahlström, T. Carette, and E. Lindroth, *Diagrammatic approach to attosecond delays in photoionization*, *Phys. Rev. A* **86**, 061402 (2012).
- [19] K. Codling and R. P. Madden, *Resonances in the photoionization continuum of Kr and Xe*, *Phys. Rev. A* **4**, 2261 (1971).
- [20] D. L. Ederer and M. Manalis, *Photoabsorption of the 4d electrons in xenon*, *J. Opt. Soc. Am.* **65**(6), 634 (1975).
- [21] J. C. A. Barata, L. F. Canto, and M. S. Hussein, *New asymptotic formulae for the point Coulomb phase shift*, *Brazilian J. Phys.* **41**, 50 (2011).
- [22] J. Dahlström, D. Guénot, K. Klünder, M. Gisselbrecht, J. Mauritsson, A. L. Huillier, A. Maquet, and R. Taïeb, *Theory of attosecond delays in laser-assisted photoionization*, *Chem. Phys.* **414**, 53 (2012).